Spectroscopy of the breaking bond: the diradical intermediate of the ring opening in oxazole

Lori M. Culberson, Adam A. Wallace, Christopher C. Blackstone, Dmitry Khuseynov and Andrei Sanov*

Bond breaking is a challenging problem in both experimental and theoretical chemistry, due to the transient nature and multi-configurational electronic structure of dissociating molecules. We use anion photodetachment to probe the diradical interactions in the ring-opening reaction of oxazole and obtain a self-consistent picture of the breaking bond. Starting from the closed-shell cyclic molecule, the reaction is launched on the anion potential, as an attached electron cleaves a carbon–oxygen bond. In the photodetachment, two neutral potential regions are sampled. One corresponds to a completely dissociated bond, while the other – to the bond fragments separated by approximately 3 Å. At this chemically relevant distance, signatures of lingering through-space interactions between the radical centers are observed.

1. Introduction

The making and breaking of covalent bonds is the essence of chemistry. It is also (arguably) the most challenging problem within the discipline. The difficulty stems from the complexity of the electronic structure—even for well-behaved closed-shell molecules—in the transient regime of emerging or breaking bonds.

Many spectroscopic and theoretical methods exist for the characterization of closed-shell molecules and their fragments (Fig. 1a, reaction stages 1 and 3, respectively). In this work, we focus on the intermediate regime of a bond stretched far from its equilibrium (Fig. 1a-2). In this case, the electronic structure assumes a diradical character,[1] dominated by the lingering interaction of the separating radicals. This interaction gives rise to several close-lying electronic states with inherently multi-configurational wavefunctions, resulting from the different ways of combining the spin and orbital contributions of the individual electrons. We employ photoelectron imaging spectroscopy to characterize the inter-radical couplings associated with a nearly-broken bond.

Although time-resolved spectroscopy[2] is usually the technique of choice to probe the transient states of dissociating molecules, we take a different approach. Rather than rushing to keep up with the fast speed of fragment separation, we exert control on the extent of bond dissociation. Specifically, in the pursuit of a breaking bond, we employ a reaction in which the fragment radicals do not separate completely, but remain at a chemically relevant distance, constrained by a larger molecular framework.

Department of Chemistry and Biochemistry, The University of Arizona, Tucson, Arizona 85721, USA. E-mail: sanov@u.arizona.edu
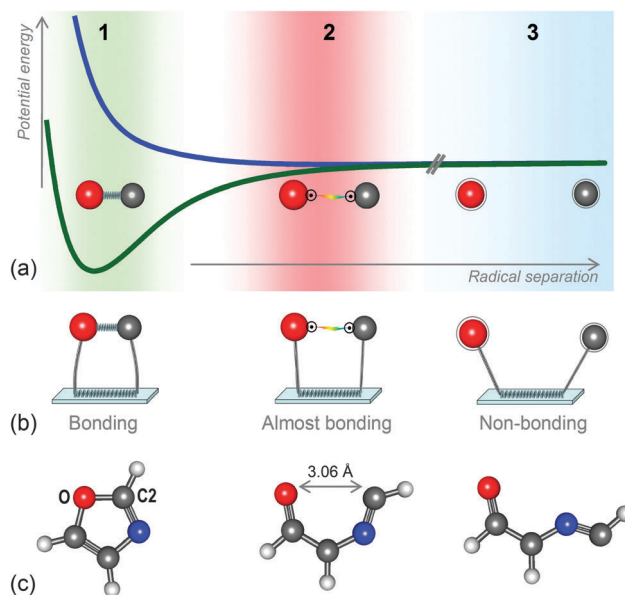
Fig. 1 Left to right: three stages of a bond-breaking reaction. (1) The intact bond near the equilibrium. (2) The nearly broken bond, with the radical fragments interacting through a narrow gap. (3) The completely broken bond, with the fragments so far apart that no direct interaction is possible. These stages are illustrated in a cartoon form for three different scenarios, (a)–(c). (a) Schematic potentials corresponding to a closed-shell molecule dissociating into free radical fragments. The regions highlighted in different colors correspond to the respective reaction stages 1–3. (b) The concept of a bond-breaking spectrometer, in which the fragments mounted on a hypothetical microscopic platform do not separate completely but remain at a controlled distance. The three states of the "spectrometer" shown correspond to respective stages 1–3 of the bond-breaking reaction. (c) Realization of the controlled bond-breaking concept from (b) using the oxazole molecule. The three molecular geometries shown correspond to stages 1–3 of the ring opening reaction along the C2–O bond.

This concept is illustrated in Fig. 1b, which represents three stages of a bond-breaking reaction with the fragments attached to a hypothetical microscopic platform: (1) the intact covalent bond; (2) the nearly broken bond, with the radicals a few Angstroms apart; and (3) the completely broken bond, with the fragments so far apart that no direct through-space interaction is possible. It is the intermediate state (2) that corresponds to the transient regime of a bond being broken (or, in reverse, formed).

This concept can be realized in a variety of ring-opening reactions, where the crucial parts of the neutral potential landscape may be accessed *via* the photodetachment of the corresponding stable anions. This approach is similar to probing neutral transition states *via* negative-ion photodetachment,[3,4] but with one important distinction: it is not a transition state that is of interest here, but the region of the reactive potential, where the diradical interactions are still significant.

We apply this idea to the ring opening in oxazole. The cyclic structure of the closed-shell molecule is shown in Fig. 1c-1. Previous studies using electron parametric resonance have shown that electron attachment cleaves the C2–O bond, forming an anion radical, in which the charge resides predominantly on the oxygen.[5,6] This reaction is indicated by pathway $1 \rightarrow 2$ in Fig. 2. Upon the photodetachment of **2**, neutral diradical **2a** is formed. Due to the vertical nature of the photodetachment, the initial geometry of **2a** is the same as that of the ring-open anion. That geometry is shown in Fig. 1c-2. As the two radical centers in the vertically accessed neutral structure interact through a small (~ 3 Å) gap, the diradical can be viewed as the intermediate state (2) of the radical-interaction spectrometer conceptualized in Fig. 1b. Chemical intuition further suggests that structure **2** in Fig. 2 may undergo a *cis–trans* internal rotation about the C4–N bond to form anion **3**. Its photodetachment results in *trans*-diradical

3a, whose relaxed geometry is shown schematically in Fig. 1c-3. With the two original bond fragments (C2 and O) far apart, the *trans*-diradical corresponds to state (3) of the Fig. 1b concept.

The anion chemistry described in Fig. 2 sets the stage for probing the diradical intermediates in the ring-opening reaction of *neutral* oxazole. The description of these intermediates must take into account the resonance of the delocalized diradical (**2a**, **3a**) and carbene (**2b**, **3b**) structures (Fig. 2). (Although carbenes—at least of the triplet kind[7]—are viewed as diradicals themselves, for clarity in this work we refer to species with two delocalized radical centers as simply diradicals, while those with two nonbonding electrons on the same carbon as carbenes.) The carbene-diradical resonance can be conceptualized as interaction of the radical centers through the intact molecular framework, indicated in Fig. 1b by the springs connecting the radical mounting posts.

Summarizing the key ideas, the relaxed cyclic structure of oxazole represents the initial state of the radical-interaction spectrometer described in Fig. 1b. In the experiment, one-electron reduction launches the molecule on the anion potential, which is initially repulsive with respect to the C2–O stretch. The ensuing ring-opening reaction yields the *cis*-anion structure (**2** in Fig. 2), separated by only a small barrier from the *trans*-potential minimum (**3** in Fig. 2). As the *trans*-anion is nearly isoenergetic with its *cis* counterpart and the isomerization barrier is smaller than the zero-point vibrational energy, the *cis* and *trans* forms of the anion exist simultaneously, with the wavefunction delocalized over the two potential minima. The photodetachment of the anion is therefore expected to probe simultaneously two regions of the neutral ring-opening landscape, corresponding to structures 2 and 3 in Fig. 1c, which represent, respectively, the nearly- and completely-dissociated states of the radical-interaction spectrometer in Fig. 1b.
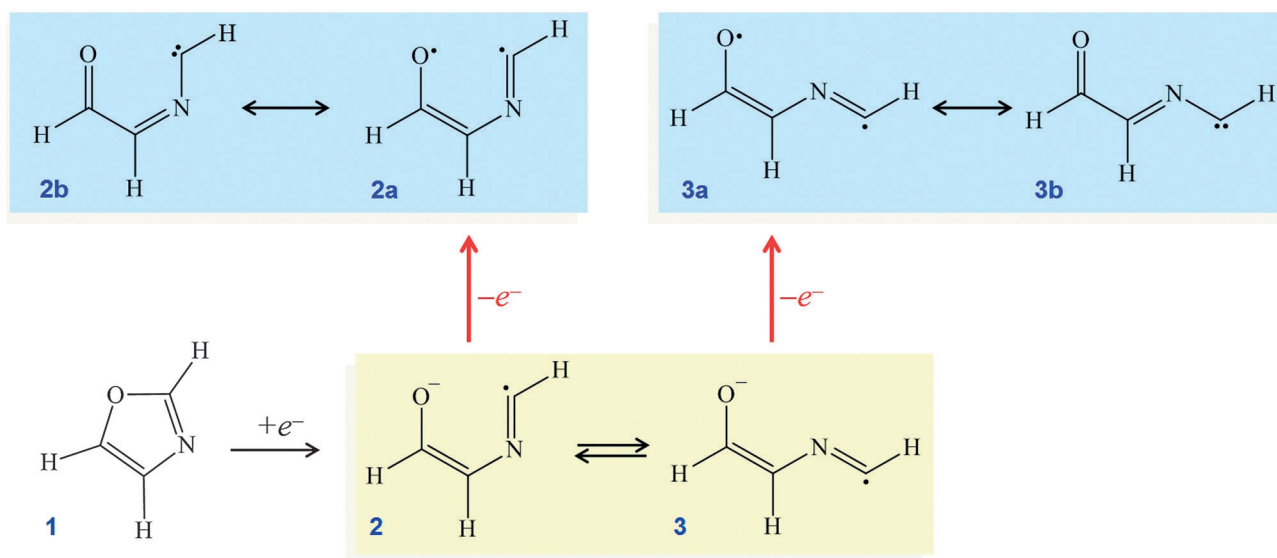

Fig. 2 Electron attachment and photodetachment pathways of oxazole. **1**: closed-shell oxazole. **2** and **3**: the *cis* and *trans* forms of the ring-open oxazole anion. **2a** and **3a**: the *cis* and *trans* ring-open neutral diradical structures. **2b** and **3b**: the *cis* and *trans* ring-open neutral carbene structures.

2. Experimental and theoretical methods

The experiments were carried out using the negative-ion spectrometer described in detail elsewhere.[8,9] The anions were generated *via* slow secondary electron attachment following the bombardment of the neutral precursor molecules with high-energy (1 keV) electrons. The precursor gas mixture consisted of room-temperature vapor of 1,3-oxazole seeded in argon carrier gas. The gas mixture was introduced into the high-vacuum chamber through a pulsed supersonic nozzle and the resulting anions were separated and characterized in the time-of-flight mass-spectrometer. Photodetachment at 532 and 355 nm was performed using the second and third harmonics, respectively, of a Nd:YAG laser. The 306 nm radiation was obtained by frequency doubling the fundamental output of a Nd:YAG pumped dye laser. The presented images correspond to multiple experimental runs, combined to span $\sim 10^6$ experimental cycles at each wavelength. The results were analyzed using the inverse Abel transformation[10] as implemented in the BASEX software package.[11]

Electronic-structure calculations involving geometry optimizations were carried out at the coupled-cluster (CCSD) level of theory using the Gaussian 09 suites of programs.[12] The low-lying electronic states of the ring-open oxazole were explored using the equation-of-motion (EOM) family of methods combined with the coupled-cluster theory.[13–16] The EOM calculations relied on the spin–flip (SF)[13] and ionization potential (IP)[16] methodologies and included the diagonal triples (dT) corrections for energy.[17] All EOM-XX-CCSD(dT) calculations (XX = SF or IP) were carried out using the Q-Chem 4.0 software package.[18]

3. Experimental results and analysis

Photoelectron images of the oxazole anion were obtained at 532, 355 and 306 nm. The corresponding photoelectron spectra, plotted *versus* electron binding energy (eBE), are shown in Fig. 3a, along with the unprocessed 355 nm photoelectron image as an example of raw data.

The spectra are broad and congested, but their appearance is not representative of the instrumental resolution. In similar experiments on cyclic anions, such as oxazolide[19] and furanide,[20] spectral resolution of several meV has been demonstrated using the same instrument, laser, and, in the case of oxazolide, the same neutral precursor. The broad and congested bands in Fig. 3a are hallmarks of the floppy structure of the ring-open anion, with a wavefunction delocalized over a large volume of the configuration space encompassing two isomers. The spectra also reflect a large equilibrium geometry change expected upon detachment to the lowest singlet surface, which correlates adiabatically with the ring-closed (cyclic) structure of oxazole.

Despite the congestion, several overlapping bands are apparent at every wavelength. The presence of distinct transitions is particularly clear in the 355 nm image included in Fig. 3a. For example, the outskirts of the image reveal at least two transitions with differing angular properties with respect to the laser polarization direction.
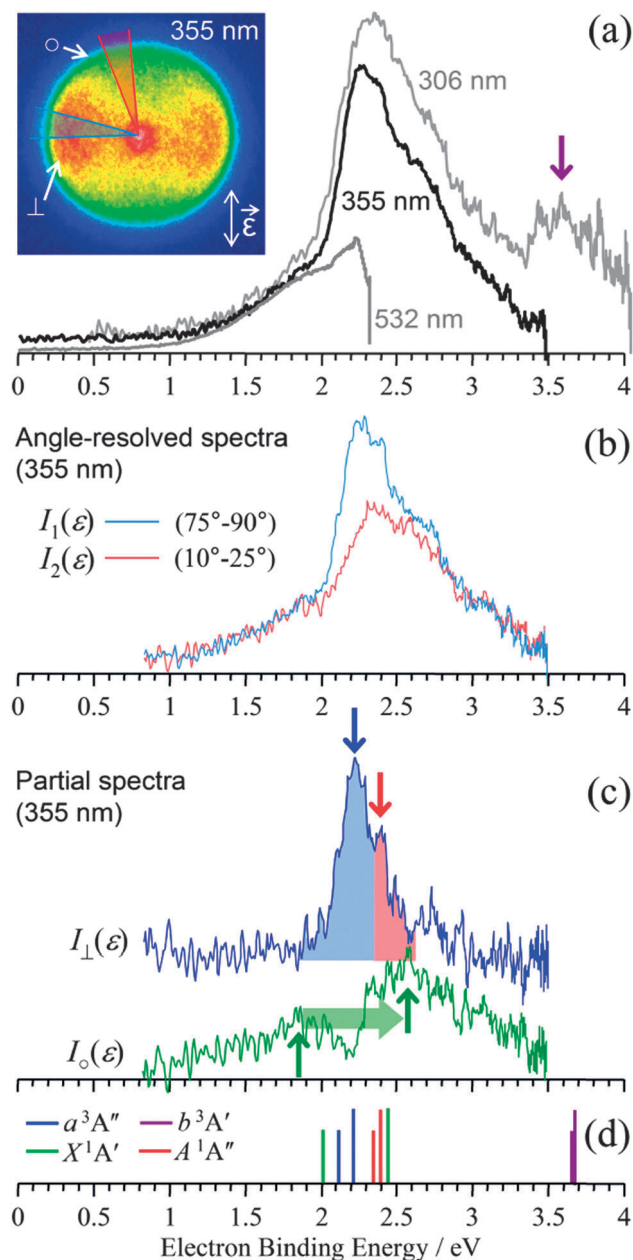

Fig. 3 Experimental results and assignment. (a) The 355 nm photoelectron image and the complete 306, 355 and 532 nm photoelectron spectra of ring-open oxazole anion. (b) The 355 nm angle-resolved spectra, $I_1(\varepsilon)$ and $I_2(\varepsilon)$, obtained by integrating the results for near-perpendicular ($\theta_1 = 75°-90°$) and near-parallel ($\theta_2 = 10°-25°$) photodetachment, respectively. The corresponding angular sectors are indicated in the image in (a). (c) The partial 355 nm spectra corresponding to the predominantly perpendicular ($\perp$) and nearly-isotropic ($\bigcirc$) transitions. All experimental spectra are arbitrarily normalized. (d) A stick spectrum based on the calculated vertical transition energies summarized in Table 2. The color scheme indicated in the legend is the same as that for the transition/state labels used throughout the paper and the band-label arrows in parts (a) and (c) of this figure.

Marked '$\bigcirc$' is an approximately isotropic band, while '$\perp$' is a predominantly perpendicular feature seen just inside the $\bigcirc$ band.

Using the photoelectron angular distributions (PAD), it is possible to deconvolute the bands with different properties.

Since the quantitative PADs are not meaningful in this case, due to the significant band overlap, we adopt the following approximate approach. Whereas the spectra in Fig. 3a were obtained by integrating the photoelectron signals over the entire angular range, Fig. 3b displays two angle-resolved spectra obtained by integrating the 355 nm image only within the respective angular sectors indicated on top of the image in Fig. 3a. For the first spectrum, the $\theta_1 = 75°–90°$ sector was analyzed, while for the second, $\theta_2 = 10°–25°$, where θ is the angle with respect to the laser polarization direction. For simplicity, in the following we collapse the above angular ranges to their respective median values, *i.e.* $\theta_1 = 82.5°$ and $\theta_2 = 17.5°$.

If $I(\varepsilon, \theta)$ is the overall energy and the angle dependent photoelectron signal, then the two angle-resolved spectra in Fig. 3b are defined as:

$$I_1(\varepsilon) \equiv I(\varepsilon, \theta_1), \quad \theta_1 = 82.5°, \tag{1}$$

$$I_2(\varepsilon) \equiv I(\varepsilon, \theta_2), \quad \theta_2 = 17.5°. \tag{2}$$

Based on the examination of the image in Fig. 3a, the overall photoelectron signal consists of two types of transitions, the predominantly perpendicular ($\perp$) and nearly isotropic ($\bigcirc$) ones. We shall accept this hypothesis and express the overall result as a sum of the partial components representing the two types of transitions:

$$I(\varepsilon, \theta) = I_{\perp}(\varepsilon, \theta) + I_{\bigcirc}(\varepsilon, \theta). \tag{3}$$

The angular dependence of each of the partial spectra is described as usual:

$$I_i(\varepsilon, \theta) = I_i(\varepsilon)[1 + \beta_i P_2(\cos\theta)], \quad i = \perp \text{ or } \bigcirc, \tag{4}$$

where β_i are the corresponding anisotropy parameter values, $I_i(\varepsilon)$ are the energy-dependent intensities of the two types of transitions (*i.e.*, the desired partial spectra), and $P_2(\cos\theta) = (3\cos^2\theta - 1)/2$ is the second-order Legendre polynomial. Although the anisotropy values are, in general, energy dependent, we shall assume them to be constant over the energy range of this analysis and based on the examination of the image ascribe the following estimated values to the $\perp$ and $\bigcirc$ transitions: $\beta_{\perp} = -0.5$ and $\beta_{\bigcirc} = 0$. The choice of these values, while qualitatively justified, is admittedly somewhat arbitrary at the quantitative level. However, all conclusions of this work are robust with respect to the $\beta_{\perp}$ and $\beta_{\bigcirc}$ choice. While adjusting these values (within reason) affects the details of the final spectra, the overall band patterns remain unchanged. Substituting eqn (4) with these β_i values into eqn (3) (once for $i = \perp$ and once for $i = \bigcirc$), we obtain:

$$I(\varepsilon, \theta) = I_{\perp}(\varepsilon)[2.5 - 1.5\cos^2\theta]/2 + I_{\bigcirc}(\varepsilon). \tag{5}$$

Recalling that the angle-resolved spectra in Fig. 3b are defined by eqn (1) and (2), we now find from eqn (5):

$$I_1(\varepsilon) = I_{\perp}(\varepsilon)[2.5 - 1.5\cos^2\theta_1]/2 + I_{\bigcirc}(\varepsilon) \tag{6}$$

$$I_2(\varepsilon) = I_{\perp}(\varepsilon)[2.5 - 1.5\cos^2\theta_2]/2 + I_{\bigcirc}(\varepsilon). \tag{7}$$

As expected, eqn (6) and (7) reveal that the angle-resolved spectra $I_1(\varepsilon)$ and $I_2(\varepsilon)$ (Fig. 3b) are linear combinations of the partial spectra $I_{\perp}(\varepsilon)$ and $I_{\bigcirc}(\varepsilon)$, representing the predominantly perpendicular and mostly isotropic bands. Conversely, rearranging this system of two linear equations allows us to express the partial spectra $I_{\perp}(\varepsilon)$ and $I_{\bigcirc}(\varepsilon)$ as linear combinations of the observed angle-resolved spectra $I_1(\varepsilon)$ and $I_2(\varepsilon)$. Specifically, with the $\theta_1 = 82.5°$ and $\theta_2 = 17.5°$ parameter values (per eqn (1) and (2)), we obtain: $I_{\perp}(\varepsilon) \propto I_1(\varepsilon) - I_2(\varepsilon)$ and $I_{\bigcirc}(\varepsilon) \propto I_2(\varepsilon) - 0.46 I_1(\varepsilon)$, where we have omitted the unimportant proportionality factors. The resulting arbitrarily normalized plots of $I_{\perp}(\varepsilon)$ and $I_{\bigcirc}(\varepsilon)$ are displayed in Fig. 3c.

In the partial spectrum highlighting the predominantly perpendicular transitions, two nearly overlapping bands are observed. Their maxima are marked with the blue and red vertical arrows. The nearly isotropic partial spectrum consists of two very broad bands. The corresponding band maxima are marked in Fig. 3c with the green vertical arrows. Finally, an additional higher-energy transition is responsible for the central spot in the 355 nm image, but best seen in the 306 nm spectrum (Fig. 3a). This transition is marked with a purple arrow.

The five color-labeled transitions and their properties are summarized in Table 1. The outermost, approximately isotropic ($\bigcirc$) ring in the image in Fig. 3a corresponds to the "green-1" band. This band is responsible for the broad low-eBE shoulders in the 306, 355 and 532 nm spectra in Fig. 3a, while the $\perp$ transitions contribute most of the intensity in the eBE = 2.0–2.5 eV range. The $\perp$ band is suppressed relative to the $\bigcirc$ shoulder at 532 nm due to the proximity to the energetic cutoff (low eKE).[21]

4. Discussion

4.1. Anion and neutral structures of ring-open oxazole

The widths of the two green bands in the $\bigcirc$ spectrum in Fig. 3c are suggestive of a large equilibrium geometry change upon the photodetachment. The $\perp$ band, on the other hand, consists mainly of two fairly narrow transitions, indicating a small geometry change.

The ring-opening potential for the ground electronic state of oxazole is represented schematically by the green curve in Fig. 4.

Table 1 Experimentally observed properties of the oxazole anion photodetachment transitions and the corresponding neutral state assignments

Transition label[a]	VDE/eV	Character ($\perp$ or $\bigcirc$)	Band width	Detachment orbital	Neutral state assignment
Blue	2.216 ± 0.009	$\perp$	Narrow	$3a''$	a^3A''[b]
Red	2.40 ± 0.02	$\perp$	Narrow	$3a''$	A^1A''[b]
Green-1	1.85 ± 0.15	$\bigcirc$	Broad	$16a'$	X^1A' (*cis*)
Green-2	2.6 ± 0.1		Broad	$16a'$	X^1A' (*trans*)
Purple	3.6 ± 0.1	$\bigcirc$	Broad	$15a'$	b^3A'[b]

[a] Transition labels correspond to the colors of the identifying vertical arrows in Fig. 3. [b] Overlapping *cis* and *trans* contributions.

This journal is © the Owner Societies 2014

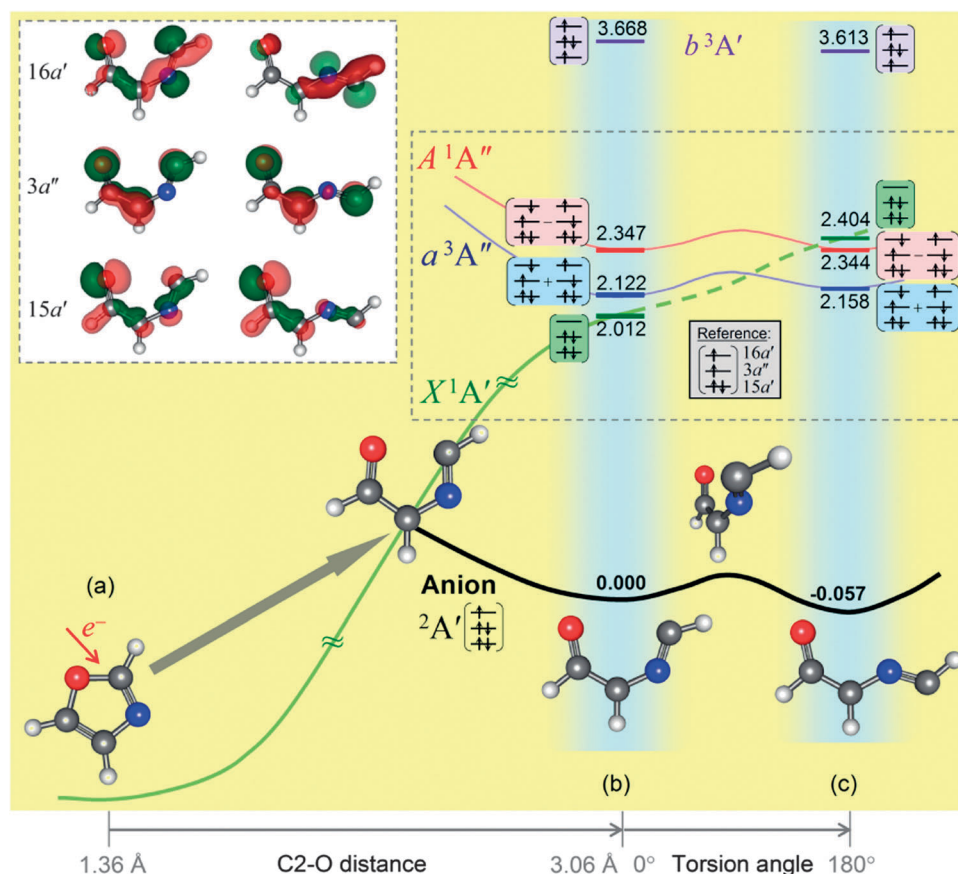*Phys. Chem. Chem. Phys.*, 2014, **16**, 3964–3972 | **3967**

Fig. 4   The electronic structure of cyclic and ring-open oxazole and its anion. (a) The ground-state cyclic structure of neutral oxazole. (b) and (c) The *cis* and *trans* minimum-energy structures of the ring-open radical anion. The green, black, blue, and red curves are qualitative representations of the ring-opening potential for the ground electronic state of oxazole (X^{1}A′), the anion (^{2}A′), and the a^{3}A″ and A^{1}A″ neutral states, respectively. The top-left inset shows the 15a′, 3a″ and 16a′ MOs for the *cis* (left) and *trans* (right) anion geometries. The neutral state energies determined from the EOM-XX-CCSD(dT)/aug-cc-pVTZ, XX = IP, SF calculations at the *cis* and *trans* anion geometries, are given in electron-volts, relative to the *cis*-anion, whereas the *cis–trans* anion adiabatic energy difference (0.057 eV) is derived from the respective CCSD/aug-cc-pVTZ geometry optimizations. The SF calculations used the M_S = 1 a^{3}A″ reference shown in the shaded (grey) inset.

Its minimum (a) corresponds to the relaxed cyclic structure with an intact C2–O bond. In the experiment, one-electron reduction launches the molecule on the anion potential, represented schematically by the black curve. That potential is initially repulsive with respect to the C2–O stretch. The minimum (b) corresponds to anion **2** in Fig. 2. To the right of this planar structure, the reaction coordinate in Fig. 4 switches to the C5=C4–N=C2 torsion angle, ranging from 0° for the *cis* structure to 180° for the *trans*. After overcoming a small barrier, the system reaches the *trans*-anion minimum (c) corresponding to anion **3** in Fig. 2.

The *cis* and *trans* geometries of the ring-open radical anion (species **2** and **3** in Fig. 2) and the corresponding neutral (**2a-2b** and **3a-3b**) were optimized at the CCSD level of theory with the aug-cc-pVTZ basis set. The optimized *cis* and *trans* anion structures are shown in Fig. 5. Also shown are the corresponding equilibrium geometries of the lowest neutral triplet state. All structures in Fig. 5 are planar and both the *cis* and *trans* anion geometries are quite similar to the corresponding triplet (a^{3}A″) structures. As perhaps the most relevant property, the C2–O distance in the *cis*-anion is predicted to be 3.06 Å, compared to 2.83 Å in the corresponding triplet structure. Both of these values represent chemically relevant

separations, corresponding to a nearly, but not completely broken bond, whereas the through-space interactions still impact the energetics and the electronic structure.

As per the CCSD/aug-cc-pVTZ calculations, the *trans* anion is 0.057 eV more stable than the *cis*, not accounting for the zero-point vibrational energy (ZPE). For comparison, the corresponding energy difference derived from B3LYP/aug-cc-pVDZ calculations is 0.082 eV, while the ZPE estimated for the *cis* anion is 0.326 eV. Furthermore, relaxed potential energy scans for the *cis–trans* isomerization indicate a barrier of only 0.092 eV (on the *cis* side). As the ZPE exceeds the barrier height, the *cis* and *trans* forms of the anion must co-exist, with the ground-state vibrational wavefunction delocalized over the two potential minima.

Hence, the topology of the anion potential energy surface is very different from the closed-shell singlet state. In contrast to the anion (and the triplet), the global minimum of the singlet corresponds to the cyclic oxazole molecule. (An additional shallow minimum was found for the singlet at a higher energy, corresponding to a non-planar ring-open geometry similar to the transition-state structure for the *cis–trans* isomerization in the anion, shown in Fig. 4. That singlet structure is also very
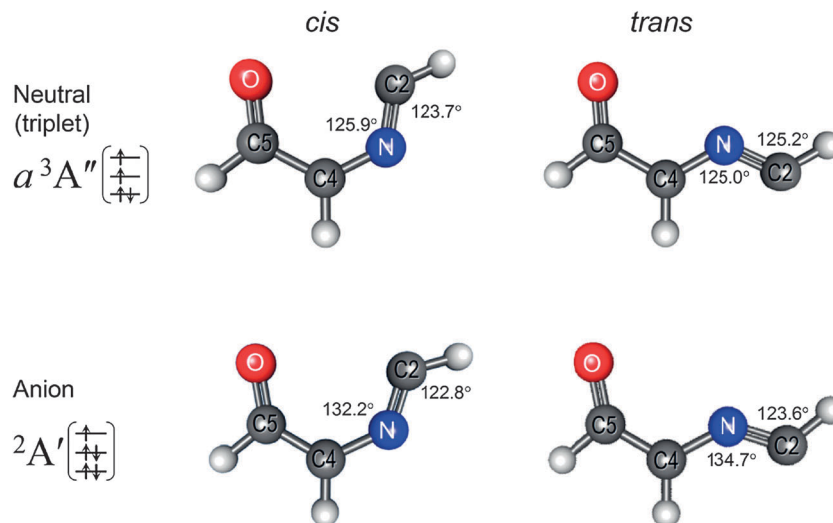
Fig. 5 The *cis* and *trans* geometries of the ring-open oxazole radical anion and the corresponding lowest-triplet neutral, optimized at the CCSD level of theory with the aug-cc-pVTZ basis set. The nominal electron configurations are indicated, with the populations corresponding to the 15a′, 3a″ and 16a′ MOs, as in Fig. 4. All structures are planar, with the key geometric parameters indicated in the figure. The *cis* structures of the triplet and the anion feature the C2–O gaps of 2.83 Å and 3.06 Å, respectively.

different from the relaxed *cis* and *trans* anion geometries and expected to undergo a ring-closing rearrangement to oxazole. Therefore, this local minimum will not be discussed further.)

Based on these results, we expect broad Franck–Condon envelopes for the $^2A'\rightarrow X^1A'$ photodetachment transitions in both the *cis* and *trans* anions. Analogous arguments based on the similarity of the triplet and anion equilibrium structures (Fig. 5) suggest narrower $^2A'\rightarrow a^3A''$ bands. Hence, we tentatively assign the two broad bands in the ○ spectrum in Fig. 3c (green-1 and green-2, per Table 1) to the respective *cis* and *trans* anion detachment to the X^1A' state, while the narrow blue and/or red bands in the ⊥ spectrum are likely due to the a^3A'' state.

The absolute energies of the relaxed anion and triplet neutral structures obtained in the CCSD/aug-cc-pVTZ calculations were used to determine the adiabatic binding energy (electron affinity) of the triplet ring-open oxazole: 1.820 eV (*cis*) and 1.882 eV (*trans*). These results are in agreement with the approximate origin of the blue band in the ⊥ spectrum in Fig. 3c.

4.2.   Electronic structure of ring-open oxazole

In order to relate the observed transitions to the diradical interactions in the ring-opening of oxazole, we consider the

key molecular orbitals (MO) involved in the reaction. The top-left inset in Fig. 4 displays the 15a′, 3a″, and 16a′ MOs for both the *cis* and *trans* anion geometries. The ordering of the orbitals may vary depending on molecular geometry and electron spin (unrestricted configurations). The nominal electron configuration of the anion ground state is $^2A'$: $\ldots(15a')^2(3a'')^2(16a')^1$ and it is the antibonding character of 16a′ with respect to the C2–O bond that is responsible for the ring-open structure of the anion. The nominal electron configurations of the low-lying singlet and triplet neutral states are summarized in Table 2.

In order to accurately describe the closed-shell singlet, triplet, and open-shell singlet states of the neutral ring-open reactive intermediate, calculations[18] using the EOM-SF and EOM-IP coupled-cluster methods[16] were carried out. In calculating the state energies, the X^1A': $\ldots(15a')^2(3a'')^2(16a')^0$ and A^1A'': $\ldots(15a')^2(3a'')^1(16a')^1$ states and the $M_S = 0$ component of the a^3A'': $\ldots(15a')^2(3a'')^1(16a')^1$ state were accessed with single spin-flip[13] excitations from the $M_S = 1$ a^3A'': $\ldots(15a')^2(3a'')^1(16a')^1$ reference (Fig. 4). The $M_S = 0$ component of the a^3A'' state was used for calculating the singlet–triplet energy gaps.[22] The reference state itself, as well as the higher-lying triplet, b^3A': $\ldots(15a')^1(3a'')^2(16a')^1$ ($M_S = 1$ only), were accessed by electron removal from the anion

Table 2 Calculated VDEs (in eV) of the ring-open oxazole radical anion (*cis* and *trans*), corresponding to detachment to the four lowest electronic states of the neutral

Neutral state	Nominal configuration and state character	VDE (*cis*)	VDE (*trans*)	Method[a]
X^1A'	$\ldots(15a')^2(3a'')^2(16a')^0$ Closed-shell singlet	2.012	2.461	EOM-IP-CCSD(dT) + EOM-SF-CCSD(dT)
a^3A''	$\ldots(15a')^2(3a'')^1(16a')^1$ Lowest triplet	2.122	2.215	EOM-IP-CCSD(dT)
A^1A''	$\ldots(15a')^2(3a'')^1(16a')^1$ Open-shell singlet	2.347	2.401	EOM-IP-CCSD(dT) + EOM-SF-CCSD(dT)
b^3A'	$\ldots(15a')^1(3a'')^2(16a')^1$ Excited triplet	3.668	3.670	EOM-IP-CCSD(dT)

[a] The single-point EOM calculations were carried out using the aug-cc-pVTZ basis set for the CCSD/aug-cc-pVTZ optimized *cis* and *trans* anion geometries shown in Fig. 5. The IP calculations were carried out by removing a beta-spin electron from the $^2A'$: $\ldots(15a')^2(3a'')^2(16a')^1$ anion reference. The SF calculations were performed starting from the a^3A'' ($M_S = 1$) reference shown in the inset in Fig. 4. The low-spin ($M_S = 0$) component of the a^3A'' state was used in calculating the singlet-triplet energy gaps. ZPE corrections are not included.

reference, using the EOM-IP methodology.[16] All calculations were carried out with the aug-cc-pVTZ basis set including the non-iterative (dT) corrections[17] to the CCSD energies. As the use of HF orbitals indicated significant spin contamination in the wave functions, unrestricted B3LYP orbitals were used for the calculations, taking advantage of the relative insensitivity of the coupled-cluster theory to the choice of orbital bases.

The resulting neutral state energies, for the *cis* or *trans* anion geometries, are represented in Fig. 4, with all numeric values given relative to the *cis*-anion equilibrium. Table 2 lists the corresponding vertical detachment energies (VDEs), determined relative to the anion at the respective *cis* or *trans* geometry. These results can be directly compared to the experimental findings. Fig. 3d shows a stick spectrum compiled from the four predicted vertical detachment transitions for each of the *cis* and *trans* anion geometries (using the VDEs in Table 2). The lines are color-coded according to the neutral state labels used throughout. The short sticks in Fig. 3d represent the *cis*-anion detachment, while the tall ones – the *trans*. The relative heights reflect qualitatively the greater population expected for the slightly more stable *trans* anion minimum.

4.3. Band assignments

The overall pattern agreement of the theoretical spectrum in Fig. 3d with the experimental spectra in Fig. 3a and c is quite remarkable. Backed by the analysis of other band properties (discussed below), it allows for consistent band assignments, summarized in Table 1.

The transition energies for all neutral states, except X^1A', are predicted to be within ~ 0.1 eV for the respective *cis* and *trans* anion structures. Accordingly, the *cis* and *trans* components of these transitions are not resolved in the experimental spectra due to the band congestion and overlap. However, for the closed-shell singlet state, X^1A', the theory predicts a significant increase in the detachment energy for the *trans*-anion relative to the *cis*.

It is this state that correlates adiabatically with the global-minimum cyclic structure of neutral oxazole. Its shift to higher energy from the *cis* to *trans* structure reflects the evolution from the almost broken to completely dissociated C2–O bond. This trend is represented by the schematic X^1A' potential curve (green) in Fig. 4. In the experiment, the two maxima in the ○ spectrum (Fig. 3c) reflect this band shift, as indicated by the horizontal block arrow. The relative intensities of the two green bands reflect the greater population expected for the *trans* anion.

The notable energy difference between the *cis* and *trans* structures on the X^1A' surface might seem unexpected at first, because of the similarity of the respective bonding patterns. The main difference between the two structures is the magnitude of the through-space interaction of the C2 and O bond fragments. This interaction is more significant in the *cis* structure, characterized by a relatively small gap between the two radical centers, compared to the *trans*, where the broken bond fragments are not in each other's proximity. Therefore, the observed band shift (the block arrow in Fig. 3c) is a signature of the breaking bond.

The X^1A' state is accessed by removing an electron from the in-plane 16a' orbital. As this orbital is responsible for the ring

opening, the $(16a')^{-1}$ detachment, in reverse, causes a significant geometry change from the anion to the neutral. This change results in broad Franck–Condon profiles of the corresponding transitions, consistent with the properties of the green bands (Fig. 3c and Table 1). Similar arguments apply to the b^3A' state, accessed *via* $(15a')^{-1}$ detachment, and the corresponding purple band in the 306 nm spectrum (Fig. 3a).

The lowest-triplet (a^3A'') and open-shell singlet (A^1A'') states, on the other hand, are both accessed by removing an electron from the mostly non-bonding out-of-plane 3a'' MO, leaving the 16a' population nominally unchanged. Hence, the topology of the a^3A'' and A^1A'' potentials and the corresponding relaxed structures are expected to be similar to each other and those of the anion. The schematic potential energy curves of the a^3A'' and A^1A'' states in Fig. 4 that mimic the qualitative features of the anion potential illustrate this prediction. These considerations favor relatively narrow a^3A'' and A^1A'' photodetachment bands, consistent with the properties of the blue and red transitions in the ⊥ spectrum in Fig. 3c.

Finally, the observed PADs are also in agreement with the above assignments. Photodetachment from π orbitals usually yields predominantly perpendicular PADs.[23,24] Therefore, the ⊥ character of the blue and red transitions is consistent with the assignment of these bands to detachment from the 3a'' orbital (the a^3A'' and A^1A'' neutral states). Photodetachment from in-plane hybrid orbitals is generally expected to fall in-between the limiting s and p cases,[25,26] known to yield parallel and predominantly perpendicular PADs, respectively. That is, the hybrid-orbital PADs gravitate towards small or zero anisotropy.[27,28] The ○ character of the green and purple bands is therefore consistent with the detachment from the respective 16a' and 15a' MOs.

4.4. Carbene–diradical interactions

Based on their character with respect to the (broken) C2–O bond, the 15a', 3a'', and 16a' MOs for the *cis* ring-open oxazole geometry (inset in Fig. 4) might be described as σ, π, and σ* orbitals, respectively. It is intriguing that the HOMO of the ring-open anion (16a') is a σ*, rather than a π* orbital. In the ring-open structure of oxazole, the π* (4a'') orbital lies higher in energy than the σ* (16a') orbital and remains unoccupied in all anion and neutral states discussed in this work.

In addition, interesting (anti-) parallels exist between the spectroscopic properties of ring-open oxazole and canonical carbenes. Such a comparison is relevant, because two of the four structures of ring-open oxazole in Fig. 2 can be described as carbenes (**2b** and **3b**), with C2 as the carbene center. As summarized above, the ground state of the oxazole anion can be viewed as a $...\pi^2\sigma^{*1}$ state. The photodetachment from the sigma-type (16a') HOMO yields the closed-shell singlet neutral, whose equilibrium geometry is very different from the anion structure. The singlet photodetachment transition in oxazole therefore results in a broad photoelectron band. The triplet neutral is formed in the detachment from the π (3a'') orbital, with a relatively small geometry change, yielding a correspondingly narrow photoelectron band.
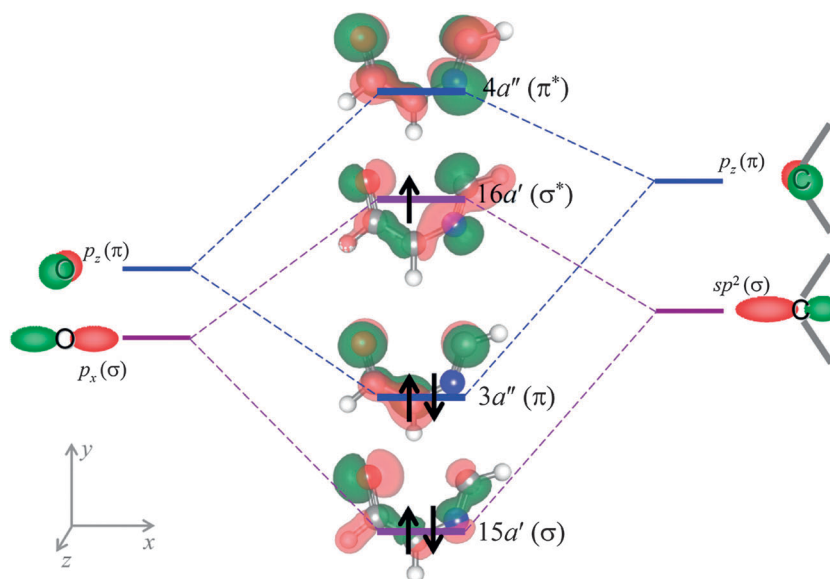
3970 | *Phys. Chem. Chem. Phys.*, 2014, **16**, 3964–3972

This journal is © the Owner Societies 2014

Fig. 6 Interaction between the relevant orbitals on the oxygen (left) and the C2 center (right) in ring-open oxazole. The resulting MOs are indicated in the middle, superimposed with the plots of the computed 15a′, 3a″, 16a′ and 4a″ orbitals of ring-open oxazole. The MO populations correspond to the anion. The schematic diagram indicates that the ...$(\sigma)_2(\pi)^1$ electron configuration of a canonical carbene anion (right) is replaced by the ...$(\sigma)^2(\pi)^2(\sigma\star)^1(\pi\star)^0$ configuration of the ring-open anion of oxazole, where the bonding and anti-bonding (*) character of the MOs are assigned solely with respect to the C2–O bond.

These observations contrast the typical carbene-anion photodetachment scenario.[7,29–34] The electron configuration of a canonical carbene anion is ...$\sigma^2\pi^1$ (not ...$\pi^2\sigma^1$), corresponding to a $^2A''$ state in the case of C_s symmetry (rather than $^2A'$ for oxazole). The closed-shell singlet state of the corresponding neutral results from the removal of a π electron, with a small geometry change and a typically narrow singlet band. The triplet carbene, on the other hand, is formed via σ detachment, resulting in a large geometry change and a broad Franck–Condon envelope of the transition.

These differences between ring-open oxazole and carbenes can be understood in terms of the interaction of the "diradical" and "carbene" structures in Fig. 2 (**2a** ↔ **2b** and **3a** ↔ **3b**). Fig. 6 illustrates schematically the effect of the interaction between the relevant orbitals on the oxygen (left) and C2 (right). For the *cis* geometry, we expect some through-space interaction across a ∼3 Å C2–O gap, in addition to the through-bond interaction via the intact molecular framework. For the *trans* geometry, the direct through-space interaction between O and C2 is no longer possible, but the through-bond interaction is expected to be similar to the *cis* structure.

The electron populations in Fig. 6, center, correspond to the ring-open anion, specifically the *cis* structure, but similar arguments apply to the *trans*-anion as well. The atomic orbitals on the left represent the O^- center, while the non-bonding σ (sp^2) and π (p) orbitals on the right represent the carbene (C2). The MOs expected from the interaction of these orbitals are indicated in the middle, superimposed with the plots of the computed 15a′, 3a″, 16a′ and 4a″ orbitals of ring-open oxazole.

As seen from the diagram, the ...$\sigma^2\pi^1$ electron configuration of a canonical carbene anion, where σ and π are the non-bonding

carbene orbitals on the right, is replaced by the ...$\sigma^2\pi^2\sigma\star^1\pi\star^0$ configuration of the ring-open anion of oxazole, where the bonding and anti-bonding characters of the MOs are assigned solely with respect to the broken C2–O bond. However, most of the bonding stabilization or antibonding de-stabilization in these MOs comes from the through-bond interaction across the intact molecular skeleton, rather than the spatial gap between the O and C2 centers. This interaction destabilizes the 4a″ MO ($\pi\star$), relative to 16a′ ($\sigma\star$), resulting in the given configurations of the ring-open anion, the corresponding neutral states, the observed spectral features, and the contrasting properties of the oxazole and carbene anion transitions.

5. Summary

All key properties of the observed photodetachment transitions in the ring-open oxazole anion agree with the theoretical predictions and the resulting self-consistent picture, summarized in Fig. 4, lends confidence in the overall description of the electronic structure of the neutral diradical. Backed by the theoretical analysis, the experiment has provided snapshots of this reactive intermediate, predominantly for two crucial geometric structures: one corresponding to the nearly broken aromatic ring, and the other corresponding to a completely dissociated C2–O bond. Together with the closed-shell structure of cyclic oxazole,[5,35,36] these structures exemplify the three key states of the general bond-breaking reaction: intact, nearly broken, and completely broken covalent bonds. The act of bond breaking itself is clearly manifest as the *cis–trans* energy shift of the closed-shell singlet band.

This journal is © the Owner Societies 2014

Phys. Chem. Chem. Phys., 2014, **16**, 3964–3972 | 3971

Acknowledgements

References

1 L. Salem and C. Rowland, *Angew. Chem., Int. Ed. Engl.*, 1972, **11**, 92.

2 A. H. Zewail, *J. Phys. Chem. A*, 2000, **104**, 5660.

3 D. N. Neumark, *Science*, 1996, **272**, 1446.

4 D. M. Neumark, *Phys. Chem. Chem. Phys.*, 2005, **7**, 433.

5 I. J. Turchi and M. J. S. Dewar, *Chem. Rev.*, 1975, **75**, 389.

6 P. H. Kasai and D. Mcleod, *J. Am. Chem. Soc.*, 1973, **95**, 27.

7 H. Tomioka, *Acc. Chem. Res.*, 1997, **30**, 315.

8 E. Surber and A. Sanov, *J. Chem. Phys.*, 2002, **116**, 5921.

9 R. Mabbs, E. Surber and A. Sanov, *Analyst*, 2003, **128**, 765.

10 A. J. R. Heck and D. W. Chandler, *Annu. Rev. Phys. Chem.*, 1995, **46**, 335.

11 V. Dribinski, A. Ossadtchi, V. A. Mandelshtam and H. Reisler, *Rev. Sci. Instrum.*, 2002, **73**, 2634.

12 M. J. Frisch, G. W. Trucks, H. B. Schlegel, G. E. Scuseria, M. A. Robb, J. R. Cheeseman, G. Scalmani, V. Barone, B. Mennucci, G. A. Petersson, H. Nakatsuji, M. Caricato, X. Li, H. P. Hratchian, A. F. Izmaylov, J. Bloino, G. Zheng, J. L. Sonnenberg, M. Hada, M. Ehara, K. Toyota, R. Fukuda, J. Hasegawa, M. Ishida, T. Nakajima, Y. Honda, O. Kitao, H. Nakai, T. Vreven, J. A. Montgomery Jr., J. E. Peralta, F. Ogliaro, M. Bearpark, J. J. Heyd, E. Brothers, K. N. Kudin, V. N. Staroverov, R. Kobayashi, J. Normand, K. Raghavachari, A. Rendell, J. C. Burant, S. S. Iyengar, J. Tomasi, M. Cossi, N. Rega, N. J. Millam, M. Klene, J. E. Knox, J. B. Cross, V. Bakken, C. Adamo, J. Jaramillo, R. Gomperts, R. E. Stratmann, O. Yazyev, A. J. Austin, R. Cammi, C. Pomelli, J. W. Ochterski, R. L. Martin, K. Morokuma, V. G. Zakrzewski, G. A. Voth, P. Salvador, J. J. Dannenberg, S. Dapprich, A. D. Daniels, Ö. Farkas, J. B. Foresman, J. V. Ortiz, J. Cioslowski and D. J. Fox, *Gaussian 09, Revision A.1 edn*, Gaussian, Inc., Wallingford, CT, 2009.

13 A. I. Krylov, *Chem. Phys. Lett.*, 2001, **350**, 522.

14 S. V. Levchenko and A. I. Krylov, *J. Chem. Phys.*, 2004, **120**, 175.

15 L. V. Slipchenko and A. I. Krylov, *J. Chem. Phys.*, 2005, **123**, 084107.

16 A. I. Krylov, *Annu. Rev. Phys. Chem.*, 2008, **59**, 433.

17 P. U. Manohar and A. I. Krylov, *J. Chem. Phys.*, 2008, **129**, 194105.

18 Y. Shao, L. F. Molnar, Y. Jung, J. Kussmann, C. Ochsenfeld, S. T. Brown, A. T. B. Gilbert, L. V. Slipchenko, S. V. Levchenko, D. P. O'Neill, R. A. DiStasio, R. C. Lochan, T. Wang, G. J. O. Beran, N. A. Besley, J. M. Herbert, C. Y. Lin, T. Van Voorhis, S. H. Chien, A. Sodt, R. P. Steele, V. A. Rassolov, P. E. Maslen, P. P. Korambath, R. D. Adamson, B. Austin, J. Baker, E. F. C. Byrd, H. Dachsel, R. J. Doerksen, A. Dreuw, B. D. Dunietz, A. D. Dutoi, T. R. Furlani, S. R. Gwaltney, A. Heyden, S. Hirata, C. P. Hsu, G. Kedziora, R. Z. Khalliulin, P. Klunzinger, A. M. Lee, M. S. Lee, W. Liang, I. Lotan, N. Nair, B. Peters, E. I. Proynov, P. A. Pieniazek, Y. M. Rhee, J. Ritchie, E. Rosta, C. D. Sherrill, A. C. Simmonett, J. E. Subotnik, H. L. Woodcock, W. Zhang, A. T. Bell, A. K. Chakraborty, D. M. Chipman, F. J. Keil, A. Warshel, W. J. Hehre, H. F. Schaefer, J. Kong, A. I. Krylov, P. M. W. Gill and M. Head-Gordon, *Phys. Chem. Chem. Phys.*, 2006, **8**, 3172.

19 L. M. Culberson, C. C. Blackstone, R. Wysocki and A. Sanov, *Phys. Chem. Chem. Phys.*, 2014, **16**, 527–532.

20 L. M. Culberson and A. Sanov, *J. Chem. Phys.*, 2011, **134**, 204306.

21 E. P. Wigner, *Phys. Rev.*, 1948, **73**, 1002.

22 L. V. Slipchenko and A. I. Krylov, *J. Chem. Phys.*, 2002, **117**, 4694.

23 R. Mabbs, F. Mbaiwa, J. Wei, M. Van Duzor, S. T. Gibson, S. J. Cavanagh and B. R. Lewis, *Phys. Rev. A*, 2010, **82**, 011401.

24 A. Sanov and R. Mabbs, *Int. Rev. Phys. Chem.*, 2008, **27**, 53.

25 E. Grumbling and A. Sanov, *J. Chem. Phys.*, 2011, **135**, 164302.

26 A. Sanov, E. R. Grumbling, D. J. Goebbert and L. M. Culberson, *J. Chem. Phys.*, 2013, **138**, 054311.

27 L. M. Culberson, C. C. Blackstone and A. Sanov, *J. Phys. Chem. A*, 2013, **117**, 11760.

28 A. Sanov, *Annu. Rev. Phys. Chem.*, 2014, **65**, 341.

29 P. C. Engelking, R. R. Corderman, J. J. Wendoloski, G. B. Ellison, S. V. ONeil and W. C. Lineberger, *J. Chem. Phys.*, 1981, **74**, 5460.

30 K. K. Murray, D. G. Leopold, T. M. Miller and W. C. Lineberger, *J. Chem. Phys.*, 1988, **89**, 5442.

31 M. R. Nimlos, G. Davico, C. M. Geise, P. G. Wenthold, W. C. Lineberger, S. J. Blanksby, C. M. Hadad, G. A. Petersson and G. B. Ellison, *J. Chem. Phys.*, 2002, **117**, 4323.

32 S. W. Wren, K. M. Vogelhuber, K. M. Ervin and W. C. Lineberger, *Phys. Chem. Chem. Phys.*, 2009, **11**, 4745.

33 D. J. Goebbert, K. Pichugin, D. Khuseynov, P. G. Wenthold and A. Sanov, *J. Chem. Phys.*, 2010, **132**, 224301.

34 D. Khuseynov, A. R. Dixon, D. J. Goebbert and A. Sanov, *J. Phys. Chem. A*, 2013, **117**, 10681.

35 M. H. Palmer, R. H. Findlay and R. G. Egdell, *J. Mol. Struct.*, 1977, **40**, 191.

36 A. E. Obukhov and L. I. Belen'kii, *Chem. Heterocycl. Compd.*, 1999, **35**, 832.

3972 | *Phys. Chem. Chem. Phys.*, 2014, **16**, 3964–3972

This journal is © the Owner Societies 2014